Graphene-nanosheet wrapped cobalt sulphide as a binder free hybrid electrode for asymmetric solid-state supercapacitor
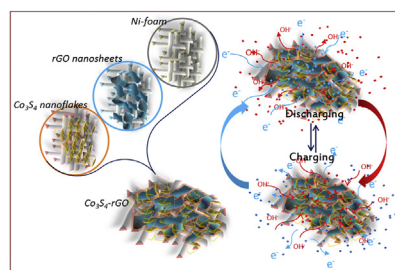
S.J. Patil [a], J.H. Kim [b], D.W. Lee [a, *]

[a] School of Mechanical Systems Engineering, Chonnam National University, 77 Yongbong-ro, Buk-gu, Gwangju 500757, Republic of Korea
[b] Department of Materials Science and Engineering, Chonnam National University, 300 Yongbong-Dong, Puk-Gu, Gwangju 500-757, Republic of Korea

HIGHLIGHTS

- Co_3S_4-rGO was synthesized by binder-free simple two-step hydro-thermal process.
- Co_3S_4-rGO electrode exhibits a high areal capacitance with ultra-high energy density.
- Co_3S_4/Co_3S_4-rGO asymmetric super-capacitor device shows a superior cyclic stability.

GRAPHICAL ABSTRACT

ARTICLE INFO

ABSTRACT

A binder-free graphene-nanosheets wrapped Co_3S_4 hybrid electrode is prepared on conductive Ni-foam via a simple two-step hydrothermal process. The physicochemical characterization such as X-ray diffraction, Raman spectroscopy, and electron microscopy revealed the formation of a Co_3S_4-rGO hybrid electrode with a large specific surface area ($30 \ m^2 \ g^{-1}$). The integrated structure of the Co_3S_4-rGO hybrid electrode exhibits an areal and specific capacitance of $8.33 \ F \ cm^{-2}$ and $2314 \ F \ g^{-1}$, respectively. The Co_3S_4-rGO hybrid electrode charges within 30 s, while the energy density remains high as $54.32 \ Wh \ kg^{-1}$ at an outstanding power density of $6.25 \ kW \ kg^{-1}$ with 92.6% excellent electrochemical cyclic stability over 1000 cycles. The asymmetric supercapacitor device is fabricated using Co_3S_4 and Co_3S_4-rGO as positive and negative electrodes, respectively, which exhibit an areal capacitance of $\sim164 \ mF \ cm^{-2}$ with reasonable cyclic stability (89.56% over 5000 cycles). The Co_3S_4/Co_3S_4-rGO supercapacitor reveals a high energy density of $1.09 \ Wh \ kg^{-1}$ at a power density of $398 \ W \ kg^{-1}$, and $0.31 \ Wh \ kg^{-1}$ energy density can be retained even at a power density of $750 \ W \ kg^{-1}$. The superior electrochemical activities of the Co_3S_4 based electrode suggest considerable promise for high-performance energy storage applications.

© 2016 Elsevier B.V. All rights reserved.

1. Introduction

Due to the rapid changes in environmental contamination, recent technologies have been focused on the development of an efficient renewable energy source and reliable energy storage devices. Supercapacitor known as electrochemical capacitors are reviewed as an important class of clean and sustainable energy storage to replace conventional capacitors and batteries thanks to their excellent electrochemical properties such as high powder and energy density, long cycling lifespan, and high discharge efficiency [1]. The supercapacitor is mainly divided into two categories which depending upon the charge storage mechanism: (i) electrical

* Corresponding author.
  E-mail address: mems@jun.ac.kr (D.W. Lee).

double layer capacitor (EDLC) and (ii) pseudocapacitor, where the electrode material plays an important role in energy storage. Carbon based materials typically show as EDLC's behavior based on electrostatic charge mechanism, and provide large specific surface area and excellent mechanical stability [2]. Generally, metal oxides and conducting polymers are utilized as a pseudocapacitive electrode material and charges are stored based on the Faradaic Redox reaction occurred at the interface of electrolyte/electrode material [3].

The electrode materials, including metal oxides, conducting polymers, metal chalcogenides, and carbon-based materials have been used as supercapacitive electrode materials. Among these categories, the good electrochemical activity and structural diversity of metal chalcogenides demonstrate it to be an attractive and promising electrode material for energy storage applications. The transitional binary and ternary metal chalcogenides, including NiS [4], CoS [5], La_2S_3 [6], MoS_2 [7], $NiCo_2S_4$ [8], etc. have received much attention as electrode materials for electrochemical applications. Amongst these, cobalt-based materials have a great deal of potential for electrochemical applications due to their multiple oxidation states and structures that enable redox reactions [9]. Cobalt sulfide (CoSx) with different stoichiometries compositions including CoS_2, Co_3S_4, CoS, and Co_9S_8 have been attracting considerable attention due to their interesting physical and chemical properties [10]. The transition phases of CoSx have been widely investigated in various applications such as magnetic materials [11], hydrogen evaluation catalysis [12], lithium ion and alkaline batteries [13], supercapacitors [5], etc.

Ghosh et al. [14] synthesized Co_3S_4 nanosheets via a two-step hydrothermal route for supercapacitor application and reported a maximum capacitance of 1369 F g^{-1} with a good electrochemical cycling stability. Chen et al. [15] synthesized Co_3S_4 nanosheet (NS) arrays via a simple shape, phase transformation route, and reported a specific capacitance of 1081 F g^{-1}. Further, Meng et al. [16] prepared cobalt sulfide/graphene by a simple hydrothermal method and reported a specific capacitance of 564 F g^{-1}. Remarkably, several researchers have reported analogous high values of capacitance close to the theoretical values (about 3000 F g^{-1}) of CoS, when the electrode material is formed on a metal current collector with lower loading mass (~5 mg) [17]. Meanwhile, it has been shown that hierarchically different micro or nanostructured materials are of great interest in material science and different approaches have been presented for the synthesis of nanostructures with complex morphology [18]. Notably, the electrochemical activities are strongly dependent on the crystalline size, porous surface microstructure, and pore size distribution of the electrode materials. Porous CoSx with pore sizes from 2 to 30 nm have been obtained in the present work by the chemical method. More interestingly, the surface area to volume ratio and pore size distribution could be controlled by adjusting the reaction temperature.

Remarkably, graphene oxide (GO) based composite electrode materials have demonstrated considerable potential for energy storage and conversion applications due to their structural features and fast reaction kinetics to manifest fully electrochemical activities [19]. The reduced functional groups of GO provide a large porous structure beneficial for improving the effective electrochemical performance of metal sulfide encapsulated with graphene-based carbonic materials [20]. The hybrid electrode enhances the structural flexibility of bare electrode, while rGO exhibited better electrochemical capacitive retention of 92.9% in Co_9S_8/graphene nanocomposites than the bare Co_9S_8 with 89.9% capacitive retention [5]. In the hierarchical Ni@Co_3S_4-rGO composite, Ni@Co_3S_4 nanosheet exhibiting a specific capacitance of 1369 F g^{-1}, anchored on the rGO hydrogel, led to a capacitance up to

1463 F g^{-1} [14]. Significantly, electrochemical performances were examined through the preparation of the hybrid electrode from the powdery material, usually using a polymeric binder and conductive agents. However, these preparation strategies affect the charge storage capacity of electrodes due to the increase in the internal resistances of the electrode and block the active sites during the electrochemical Redox reaction. The present work describes the recent progress made in designing binder free nanostructured architecture of cobalt sulphide based materials for electrochemical applications.

A binder-free strategy based on a simple two-step hydrothermal method is employed for the syntheses of Co_3S_4 and Co_3S_4-rGO electrodes on Ni-foam for supercapacitor applications. The prepared electrodes are characterized through different characterization techniques and their supercapacitive properties are systematically investigated. The excellent electrochemical performance of prepared Co_3S_4-rGO hybrid electrode highlighted the importance of the hierarchical structure of the material. Electrochemical measurements show that Co_3S_4 electrode demonstrate superior electrochemical performance with respect to Co_3S_4-rGO hybrid electrode in an asymmetric supercapacitor assembly, which can be attributed to the optimal reaction temperature and specific microstructures of the Co_3S_4 electrode.

2. Experimental details

2.1. Materials

Commercial expanded graphite, sulfuric acid (H_2SO_4), hydrochloric acid (HCl), hydrogen peroxide (H_2O_2), potassium permanganate (KMnO4), cobalt chloride ($CoCl_2 \cdot 6H_2O$), urea (CH_4N_2O), sodium sulphate (Na_2S), polyvinyl alcohol (PVA), sodium hydroxide (NaOH), and potassium hydroxide (KOH) were obtained from Sigma Aldrich Chemical Reagent Co., Ltd.

2.2. Preparation of Co_3S_4 and Co_3S_4-rGO

Graphene oxide (GO) was synthesized according to the modified Hummers method [21]. The prepared GO was reduced by precursor solution of urea using the hydrothermal method, then obtained solution was centrifuged for 5 h, and the separated product of reduced graphene oxide was collected. Co_3S_4 electrodes were prepared by a simple two-step hydrothermal method on Ni-foam. Ni-foam with a thickness of 1.6 mm was cut into 1 × 2 cm^2 pieces and etched in HCl solution (40%) for 15 min, then washed with deionized (DI) water and ethanol, and finally ultrasonically cleaned for 20 min to remove the oxide layer. The schematic diagram for the growth of Co_3S_4 nanoflakes network over Ni-foam is shown in Fig. 1. In typical synthesis process, the equimolar amount of $CoCl_2 \cdot 6H_2O$ and CH_4N_2O dissolved thoroughly in 40 ml DI water and obtained solution was stirred for 30 min with stirring rate of 430 rpm at 60 °C. The stirred solutions with Ni-foam were transferred into a Teflon-lined stainless steel autoclave. Then, Ni-foam contained Teflon-lined stainless steel autoclave kept in the oven for reaction and set hydrothermal reaction temperature as 120 °C for 10 h. After the hydrothermal reaction terminated, the oven was cooled down naturally to room temperature (RT) and take out the Teflon-lined stainless steel autoclave from the oven, and collect the samples. The light pinkish colored Co precursor coated Ni-foam samples obtained from the solution were washed with DI water and ethanol alternatively for several times. Finally, prepared Co precursor coated Ni-foam sample were dried at 70 °C for overnight. In the second step, 100 mg of Na_2S was dissolved in 40 ml of DI water under stirring of 400 rpm at 40 °C for 30 min, to which 10 mg of as-prepared Co precursor coated Ni-foam samples were
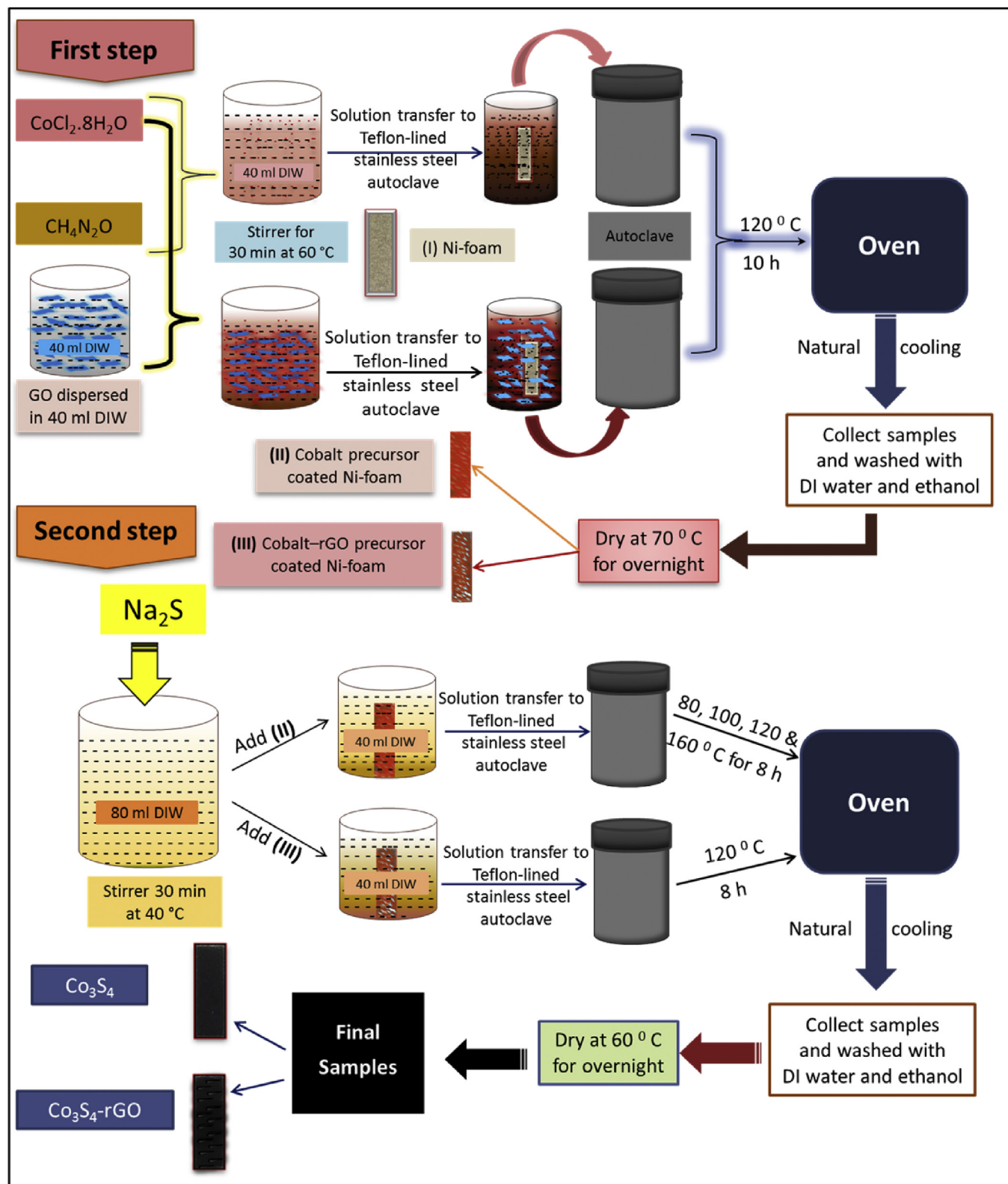
Fig. 1. Schematic illustration for the preparation of Co₃S₄ and Co₃S₄-rGO on Ni-foam using two-step hydrothermal method.

immersed into the solution. Then, the solution was further transferred to Teflon-lined stainless steel autoclave and was kept in the oven, and subsequently heated at 120 °C for 8 h for the hydrothermal reaction. When the oven was cooled down naturally (RT),

the samples were collected from the Teflon-lined stainless steel autoclave. The collected samples were washed with ethanol and DI water, and dried at 60 °C for overnight. To acquire the appropriate elemental stoichiometry and crystal structure, the second step

followed for the different hydrothermal reaction temperatures of 100, 120, and 160 °C by keeping a constant reaction time period. Finally, the prepared samples were noted as CS1, CS2, CS3, and CS4 at the hydrothermal reaction temperatures of 80, 100, 120, and 160 °C, respectively. From the EDX analyses (see Fig. 2(**a″-d″**)), it confirms that the hydrothermal reaction temperature of 120 °C (Fig. 2(**c″**)) exhibits appropriate stoichiometry (Co: S as 40.92: 59.08) and shows good electrochemical performance (Fig. 6(**a–c**)). Thus, the hydrothermal reaction temperature of 120 °C was further used for Co₃S₄-rGO hybrid electrode preparation. Briefly, 10 mg of GO was dispersed in 40 ml DI water under a stirring speed of 1000 rpm at room temperature to form a homogeneous solution. Then, CoCl₂·6H₂O was added in homogeneous solution where co-balt ions were adsorbed on the GO surface due to the electrostatic force of attraction between the cobalt ions and negatively charged oxygen-containing functional group on the GO surface (C=O, and COO−, OH). Finally, CH₄N₂O dissolved in mixture solution and stirred (430 rpm) for 30 min at 60 °C to form graphene oxide contained cobalt precursor solution. Further, Co₃S₄-rGO hybrid electrode was prepared according to the same protocol as explained earlier for the hydrothermal reaction temperature of 120 °C as depicted in Fig. 1, in which replaced the cobalt precursor solution with graphene oxide contained cobalt precursor solution.

2.3. Characterization techniques

The prepared Co₃S₄ and Co₃S₄-rGO hybrid electrode materials was characterized for their structural, morphological, and elemental analysis using various characterization techniques. Field emission scanning electron microscopy (FE-SEM; JEOL JSM-7500F) was used to study the surface morphology and elemental analysis of the electrode material. Transmission electron microscopy (TEM, HR-TEM, JEM-2100F, JEOL) was employed to characterize the microstructure of the electrode material. The crystal structure and crystallinity of the prepared electrode materials were recorded on

X-ray diffractometer (XRD; X -Pert-pro using CuKα) in the scan range of 20−90°. To check the molecular structure and phase purity of the prepared material, Fourier Transform Infrared spectroscopy (FT-IR, Bruker, EQUINOX 55/S/NIR SP spectrometer) and Raman (NRS-5100, JASCO spectrometer) analysis were performed. X-ray photoelectron spectroscopy (XPS, ESCALAB-MKII) was employed to analyze the oxidation states of the prepared material. The specific surface area measurements were carried out by the nitrogen adsorption/desorption technique based on the Bru-nauer−Emmett−Teller (BET, Micromeritics (ASAP2010)) method and the Barrett-Joyner-Halenda (BJH) method was used to obtain the pore size distributions.

2.4. Electrochemical measurements

Electrochemical properties of prepared electrodes were conducted using cyclic voltammogram (CV) and galvanostatic charge/discharge (GCD) study using an electrochemical workstation (WBCS3000) operated with WONATECH software. The electrochemical tests were carried out by dissolving the appropriate amount of salt (2 M KOH) in DI water. The three-electrode system was conducted with a saturated calomel electrode (SCE) and platinum wire as a reference and counter electrodes, respectively and the prepared electrode was used as the working electrode.

CV's were employed to calculate the areal (interfacial) and specific capacitances of the prepared electrode at various scan rates based on the following Equation (1) [6],

$$C_i = \frac{\int_{V_1}^{V_2} I(V)dV}{\nu \times (V_2 - V_1)} \text{ and } C_s = \frac{C_i}{m} \tag{1}$$

where C_i and C_s are the areal (F cm^{-2}) and specific capacitance (F g^{-1}) of electrode material, respectively, ν is the scan rate (mV s^{-1}), (V_2-V_1) is the working potential window (V), I is the current
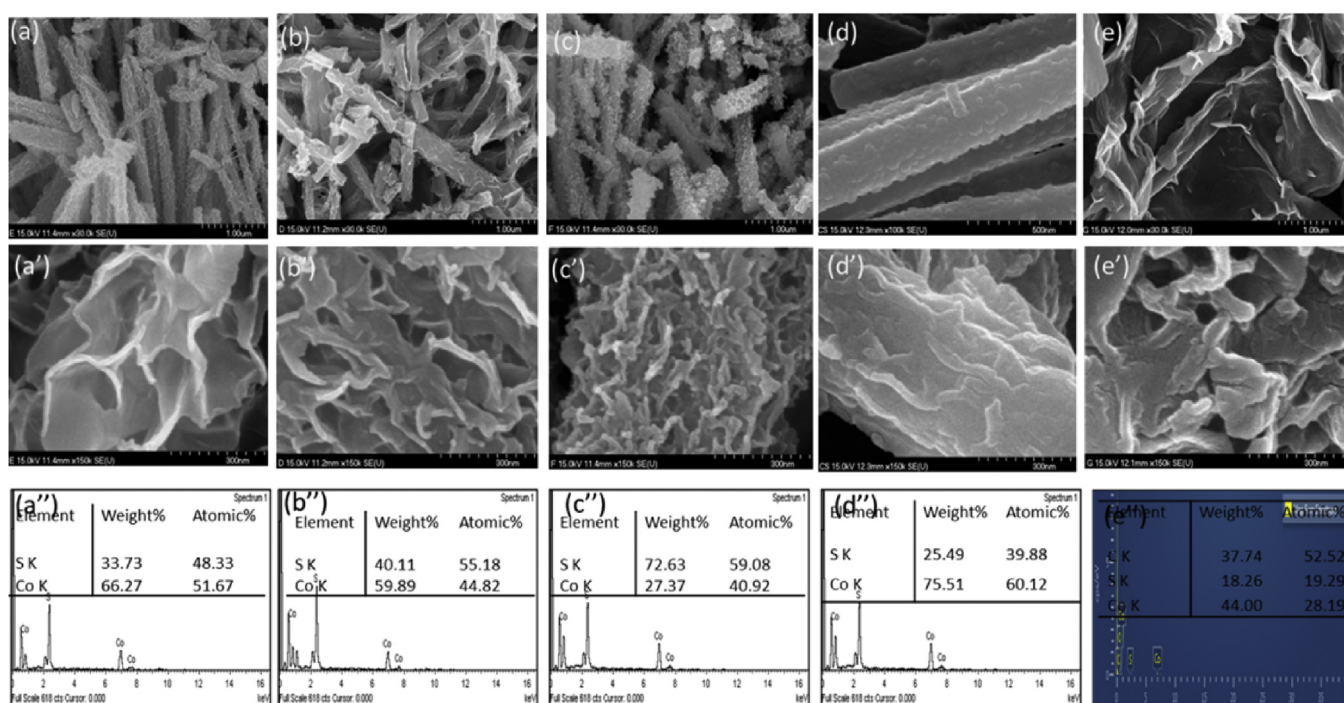

Fig. 2. FE-SEM micrographs at different magnifications for Co₃S₄: (**a-a′**) CS1, (**b-b′**) CS2, (**c-c'**) CS3, (**d-d′**) CS4, (**e-e′**) CS3-rGO samples prepared by different hydrothermal reaction temperatures (80 °C, 100 °C, 120 °C, 160 °C) and EDX pattern (**a″-e″**) with corresponding elemental composition analysis.

response (mA) of the electrode material for unit area (1 cm^2), and m is the deposited areal mass of electrode material. Further for the Ragone plot, specific energy density (E), and specific power density (P) was evaluated from the charge—discharge profile using the following Equation (2),

$$C_{cd} = \frac{I \times Td}{(V_2 - V_1) \times m}, \ E = \frac{0.5 \times C_{cd} \times (V_2 - V_1)^2}{3.6} \text{ and } P$$
$$= \frac{E \times 3600}{Td} \tag{2}$$

Where C$_{cd}$ and Td are the discharging specific capacitance (F g^{-1}) and discharging time (s), respectively, I (mA cm^{-2}) is the applied working charge/discharge current, (V$_2$−V$_1$) is a potential window range (V) during the charge/discharge cycle. The areal mass loading of electroactive material on the Ni-foam is approximately 3.2 mg and 3.7 mg for Co$_3$S$_4$ and Co$_3$S$_4$-rGO, respectively, calculated using the weight difference method. The electrochemical impedance analyses were conducted using three electrode configurations in 2 M KOH electrolyte solution by applying an AC voltage with 10 mV amplitude in a frequency range from 1 MHz to 0.1 Hz.

3. Results and discussion

3.1. Microstructure studies

FE-SEM surface morphological micrographs of Co$_3$S$_4$ and Co$_3$S$_4$-rGO hybrid electrode material are presented in Fig. 2. The length of each nanoflake can be well controlled through the hydrothermal reaction temperature by maintaining a constant reaction time. At lower magnification, the Co$_3$S$_4$ electrode surface exhibits a micro-rod which consisting of dense nanoparticles (Fig. 2(a—d)). On the other hand, at higher magnification, dense nanoparticles forming the interconnected nanoflakes are grown on Ni-foam (see in Fig. 2(a'-d')). From the FE-SEM micrographs of the Co$_3$S$_4$ material, the particle size decreases with the reaction temperature. Fine, uniform, and stable surface is observed for 120 °C hydrothermal reaction temperature (Fig. 2(c)). The porous surface morphology composed of an interconnected nanoflakes framework with the presence of mesoporous is shown in Fig. 2(c) and (c'). Such nanostructured morphology is extremely useful in electrochemical application, especially in supercapacitors to store a large amount of charge. The smaller particle size with the porous surface can be expected to achieve an effective surface area.

The formation of rGO-nanosheet wrapped Co$_3$S$_4$-nanoflakes directly on the Ni-foam in Co$_3$S$_4$-rGO frameworks are schematically presented in Fig. 3. The graphene oxide was used as a template for heterogeneous nucleation and direct growth of Co$_3$S$_4$ on the Ni-foam surface. Cobalt ions directly bond to the negatively charged oxygen atoms via an intermolecular bond, which adsorbs and directly grown on the GO nanosheets and GO was reduced to rGO at the same time. The graphene sheets assist as a framework of a conductive network that ensures to shorten the diffusion length for electrolyte ion migration and improved rate performance of the active material. The cobalt ions can adsorb the functional group of graphene oxide and made good interfacial contact between them to improve the surface area accessibility of electrode around the electrolyte ion. Fig. 2(e) and (e') suggest that rGO nanosheets wrapped nanoflakes, providing the connective path for ion diffusion.

TEM analyses are performed to provide more insight into the morphological and microstructure of the Co$_3$S$_4$ and Co$_3$S$_4$-rGO hybrid electrodes. As seen in Fig. 4(a—c), Co$_3$S$_4$ consists of a randomly aggregated uniform thin distribution of nanoflakes

showing close restocking. TEM microstructure of the Co$_3$S$_4$ electrode shows the nanoflake-like surface microstructure (Fig. 4(a)); while introducing graphene, the structure of nanoflakes converts into several nanosheet-layers of graphene that could provide a conductive network and fast ion diffusion pathways for redox reactions as seen in Fig. 4(f). The Co$_3$S$_4$ nanoflakes fully covered with rGO nanosheets are clearly seen in the TEM image (Fig. 4(f—h)). The TEM image of Co$_3$S$_4$-rGO also supports FE-SEM analysis of the nanoflakes morphology of Co$_3$S$_4$ covered with the rGO. Selected area electron diffraction (SAED) patterns are shown in Fig. 4(e) and (j) that exhibit the polycrystalline structure of Co$_3$S$_4$ and Co$_3$S$_4$-rGO. The presence of spots, as well as ring in the SAED pattern confirms that the growth of Co$_3$S$_4$ nanoflakes occurs from the rGO. Also, the diffraction rings can be indexed to the (311), (400), (440), and (533) planes of Co$_3$S$_4$, being in good agreement with the obtained XRD results. The HR-TEM image of the Co$_3$S$_4$-rGO nanosheets gives a lattice spacing of 0.33 nm and 0.178 nm, corresponding to the (311) and (440) interplanar spacing, respectively (Fig. 4(d) and (i)).

The resulting distribution of the component in the Co$_3$S$_4$-rGO materials is further evaluated by the energy-dispersive X-ray spectroscopy (EDX) mapping technique as shown in Fig. 4(k-n), where the compositional analysis of the composite material gives C, Co, and S contents. The significant differences in EDX spectrum of the Co$_3$S$_4$ electrode have been observed as supported in the XRD study, while the peak intensities of Co and S considerably changed with the changed reaction temperature (see Fig. 2(a''-d'')). Fig. 2(e'') shows the EDX spectrum of Co$_3$S$_4$-rGO with atomic % of C, Co and S. Inset of Fig. 2(a''-d'')) present the elemental composition analysis that exhibits the change in atomic % of Co and S. With increase the hydrothermal reaction temperature, the sulfur ion concentration (%) increases and at 120 °C reaction temperature there was appropriate formation of Co$_3$S$_4$ phase. After the 120 °C hydrothermal reaction temperature, sulfur concentration decreases due to the decomposition of sulfur. Fig. 4(l—n) clearly show homogeneous and continuously distributed C, Co, and S elements that could be enhancing the ion transport kinetics of the electrode. This phenomenon promotes ion transfer into the interior pore to obtain superior electrochemical performance.

3.2. Structural studies

The XRD patterns of prepared Co$_3$S$_4$ and Co$_3$S$_4$-rGO material are shown in Fig. 5(a). The XRD patterns suggest that the major diffraction peaks at a 2θ angle of 31.49°, 38.47°, 50.68°, 55.30°, 65.18°, 68.99°, and 82.32° correspond to the peaks of (311), (400), (511), (440), (533), (444), and (800), respectively, are well matched with the standard JCPDS card (00-002-0825) of cubic type Co$_3$S$_4$ [14]. These XRD patterns with the single phase of Co$_3$S$_4$ material exhibit a cubic crystal structure. The crystallite size of ~12 nm is calculated using the Scherer formula by fitting the most intense peak of the Co$_3$S$_4$ material. The inset in Fig. 5(a) shows a broad peak with the peak centered at 2θ = 24.03° (starting 2θ from 13° to 32°), confirming the reduction of graphene oxide and the peak at 43° due to the disordered carbon materials [22]. The Co$_3$S$_4$-rGO electrode presents all the peaks indexed to be the cubic Co$_3$S$_4$ structure, and an extra diffraction peak is observed at 24.71° attributed to the (002) peak for rGO. FT-IR spectroscopy studies of the Co$_3$S$_4$, rGO, and Co$_3$S$_4$-rGO electrode material are carried out separately to identify the characteristic functional group and confirmation to the formation of the prepared hybrid material, the results of which are shown in Fig. 5(b). The IR band appears at 632 and 1021 cm^{-1}, which are assigned to C—S in the stretching vibration modes [23]. The strong band at 3442 cm^{-1} corresponds to the stretching vibration of NH$_2$. Reduced graphene oxide exhibits characteristic absorption peaks of oxygen-containing groups (Fig. 5(a), spectrum
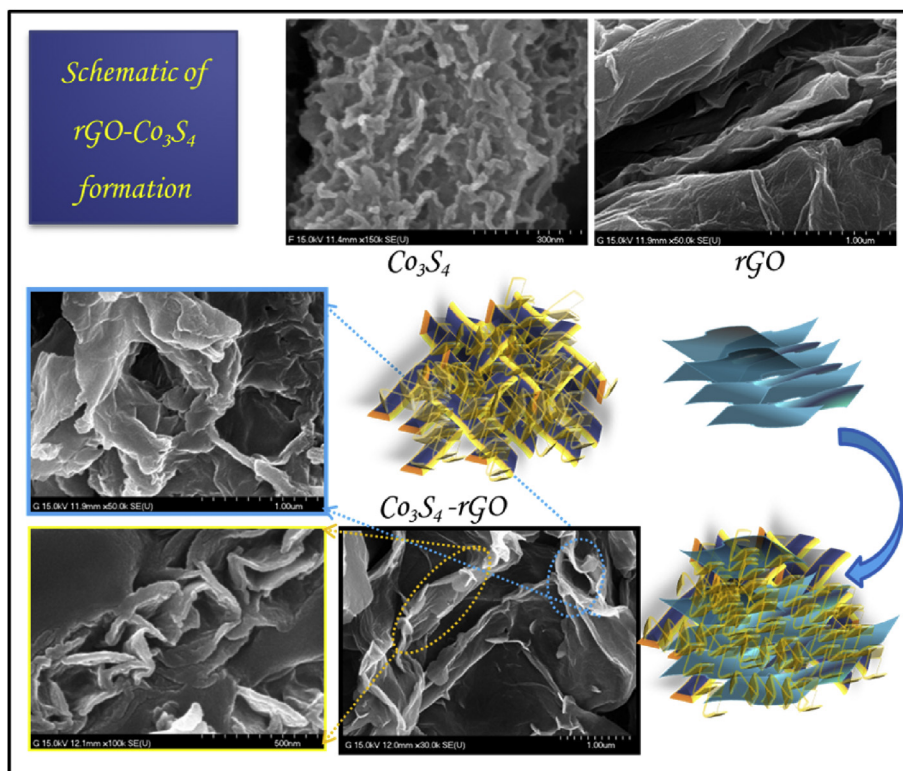
Fig. 3. Schematic drawing with FE-SEM micrographs of rGO and Co_3S_4 for the formation of Co_3S_4-rGO hybrid structure on a Ni-foam surface.

(ii)). The absorption bands include 1107 cm^{-1} for C—O stretching vibrations [24], 1635 cm^{-1} for skeletal vibrations from graphitic domains [24], 1720 cm^{-1} for C=O stretching vibrations from carbonyl and carboxylic groups [24]. Spectrum (iii) in Fig. 5(**b**) shows the FT-IR measurement for Co_3S_4-rGO, a rGO spectrum with weak intensity, and the disappearance of the oxide functional group indicates the reduction of graphene oxide. The observed absorption band at 1176 cm^{-1} disappears and absorption at 1114, 1553, 1877, 2108, and 2339 cm^{-1} indicates that the carbon-oxygenated functional groups are successfully reduced [25]. Also, the peaks observed at 890 and 1080 cm^{-1} are assigned to the epoxy vibrations in graphene oxide [26]. Fig. 5(**c**) presents the Raman spectra of Co_3S_4, rGO, and Co_3S_4-rGO material obtained at room temperature. The spectra are collected in a wavenumber range from 100 to 2000 cm^{-1}. The main characteristic Raman peaks of Co_3S_4 lie at 648.43 cm^{-1} are assigned to the A1 mode. In addition, spectrum (i) exhibits characteristic peaks at 453 and 522 cm^{-1}, corresponding to the Eg and F2g modes of the asymmetric emission bands, respectively [27]. Nearly all Raman peaks observed in the spectral range between 450 and 750 cm^{-1} are consistent and well matched with previously reported values for CoS [28,29]. This suggests that the CoS particles have good crystallinity. The reduced graphene oxide (spectrum (ii)) represents the Raman shifts at 1363 and 1590 cm^{-1}, corresponding to the intensity of defect (sp3) related to the disordered band (D-band) and sp2 hybridization related to the graphitic band (G-band), respectively, of carbon-based materials [30]. Co_3S_4-rGO spectrum (iii) consisting of carbonous high-intensity bands of D and G corresponds to the breathing mode of the κ-point phonons of A1g and tangential stretching mode of the E2g phonons of sp2 atoms [31] and a minor peak of CoS, confirming the presence of graphene and CoS. The intensity ratio of I_D/I_G increased in Co_3S_4-rGO is due to the graphene nanosheets promoted by the intercalation of CoS [32].

To explore the surface electronic structure, chemical bonding, and composition of Co_3S_4-rGO, X-ray photoelectron spectroscopy (XPS) analysis is carried out. Fig. 5(**d**) shows the typical XPS full scan spectrum of Co_3S_4-rGO. The figure clearly shows that the XPS spectrum can be fitted with the peak components that prove the presence of the elements of C1s, O1s, Co2p, and S2p. Fig. 5(**e**) shows the C1s XPS spectrum for Co_3S_4-rGO has a major peak at 284.7 eV corresponding to sp2-hybridized graphitic carbon (C—C) [33], showing the majority of carbon atoms. Additional minor peaks appear at 285.56 eV and 287.67 eV, corresponding to graphitic sp2 carbon atom C—O and O—C—O bonds. However, the component at 291.3 eV is assigned to carboxylate carbon C(O)OH [34]. The C1s spectrum suggests the presence of oxygen functional groups due to the appearance of higher binding energies. The Co 2p core level spectrum is shown in Fig. 5(**f**), as it reveals the two distinct peaks at binding energies of 778.39 eV and 793.23 eV attributed to Co 2p3/2 and Co 2p1/2, respectively, indicating the existence of the Co2+ and Co3+ valences in the material [35]. The difference between the binding energy values of the Co 2p3/2 and Co 2p1/2 levels is derived from spin—orbit splitting and the observed spin—orbit splitting is 14.84 eV. The sulfur S 2p1/2 peak at the binding energy of 161.7 eV indicates the prepared material composed of metal—sulfur bonds (Fig. 5(**g**)). On the other hand, the peak S 2p3/2 observed at 163.5 eV corresponds to the sulfur bonded with carbon (aromatic C—S—C), suggesting that S is somehow doped in graphene nanosheets [36]. This clearly demonstrates that Na_2S provides the possibility of the simultaneous incorporation of S atoms into the reduced graphene oxide during the formation of Co_3S_4. Remarkably, the appearance of additional peaks at about 169.1 eV could be ascribed to the inconsequential number of Co_xS_y (x = 1, 2.4; y = 1, 2.9) compounds because the deposited cobalt sulfide is a non-stoichiometric compound [37].
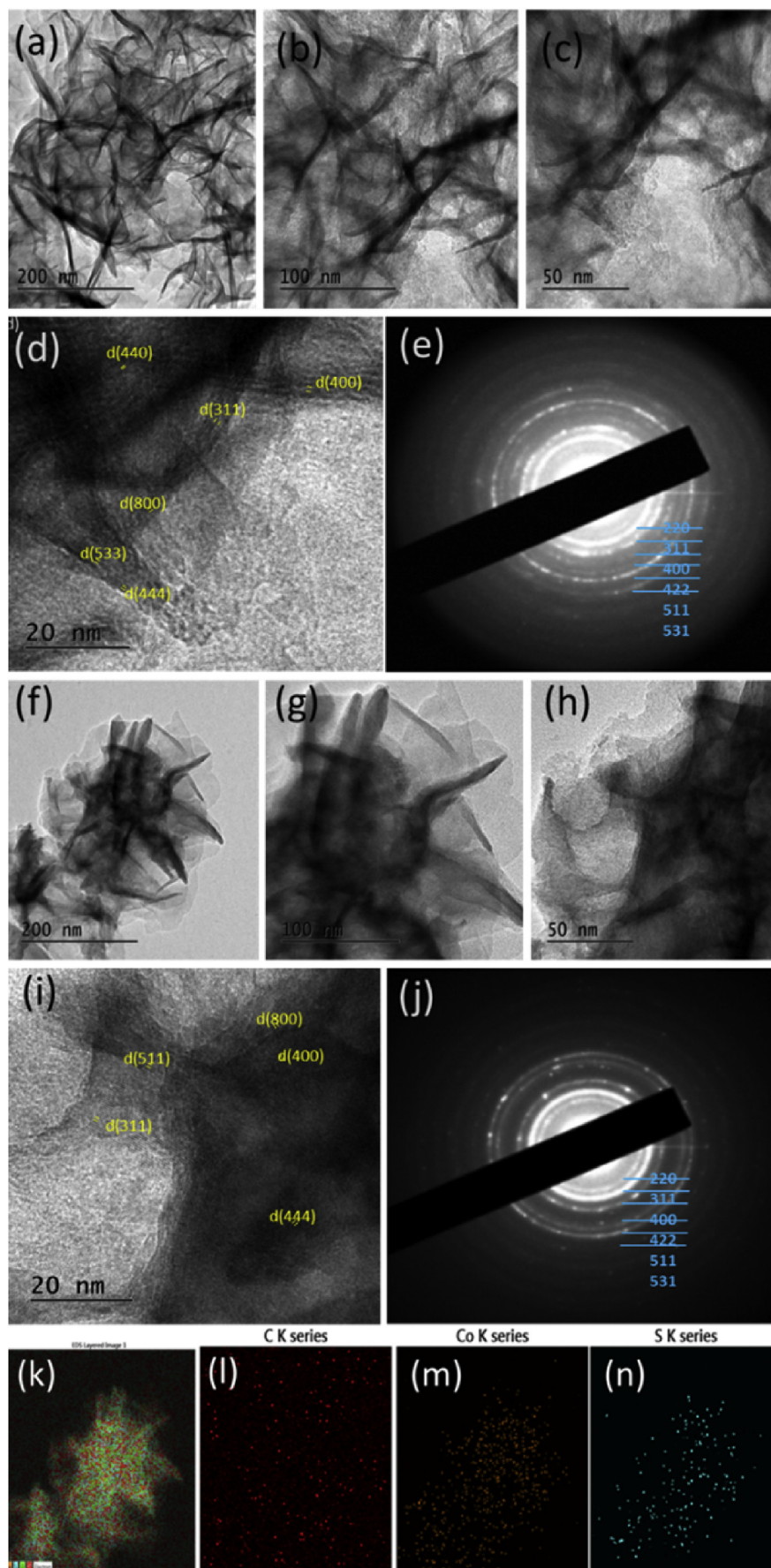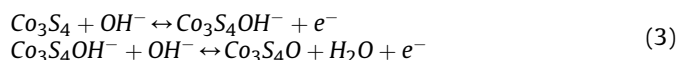
Fig. 4. TEM images of (**a**–**c**) Co_3S_4 and (**f**–**h**) Co_3S_4-rGO; scale bar 200 nm, 100 nm and 50 nm, respectively. (**d, i**) HR-TEM images with fringe spacing of Co_3S_4 and Co_3S_4-rGO hybrid particles and the corresponding SEAD pattern (20 nm scale bar) (**e, j**). FESEM-EDX elemental mapping for (**l**) C, (**m**) Co, and (**n**) S elements in Co_3S_4-rGO with rGO-nanosheet wrapped interconnected nanoflakes microarchitecture of Co_3S_4 (**k**).

3.3. BET study

The specific surface area and pore size are the most important parameters for achieving excellent electrochemical energy storage capability. N_2 adsorption–desorption isotherms are shown in Fig. 5(**h**) and (**i**) for Co_3S_4 and Co_3S_4-rGO material powder, respectively, where the inset plots show the corresponding pore size distribution. The uniform hysteresis loop profile of the prepared electrode material can be observed in the larger range of relative pressure (P/P0) illustrating that Co_3S_4-rGO has a typical mesoporous structure with a highly pores distribution in the 0–30 nm range. The specific surface area of the Co_3S_4 material is calculated to be 21 $m^2\,g^{-1}$. Fig. 5(**h**) indicates that the composite of reduced graphene oxide can increase the active specific surface area of Co_3S_4 material from 21 to 30 $m^2\,g^{-1}$. This means that the increment of the surface area results from the decrease of the particle size, which increases the active surface roughness. The Barrett–Joyner–Halender (BJH) technique was used for calculation of pore size distribution from the adsorption branches of the nitrogen isotherms. The result suggests a mesopore size distribution centered at 3.2 and 2.3 nm for the Co_3S_4 and Co_3S_4-rGO, respectively. This indicates that the Co_3S_4-rGO electrode material enhanced the electrochemical performance to an effective transport of the ions in the surface electrode. Especially, carbon-based material exhibits mesoporous architecture, which reduces the ion diffusion distance and can allow for creating more active sites that expected to enhance in energy storage capability [38,39]. The mesopore size and pore volume increased from 0.11 to 0.14 $cm^3\,g^{-1}$, revealing a fast ion pathway to achieve the good rate capability of the Co_3S_4-rGO material.

4. Supercapacitive study

Electrochemical studies are employed to characterize the capacitive performances of the Co_3S_4 and Co_3S_4-rGO hybrid electrodes. Fig. 6(**a**) shows the typical CV curve of all Co_3S_4 electrodes (CS1, CS2, CS3, and CS4) in the potential window range from −0.3–0.6 V vs. SCE at a scan rate of 50 mV s^{-1}. From the figure, it is seen that a pair of well-defined redox peaks in the Co_3S_4 electrode demonstrates that Faradic reactions can be attributed to the contribution of $Co^{2+}/Co^{3+}/Co^{4+}$ reversible Faradaic redox conversion in an alkaline electrolyte on the surface [40]. The charge storage mechanism involves adsorption of electrolytic active ions on the electrode surface diffusion and intercalation/de-intercalation of electrolyte ions. The following equation shows that the charge storage mechanism of Co_3S_4 can be shown in alkaline electrolyte [41],

$$Co_3S_4 + OH^- \leftrightarrow Co_3S_4OH^- + e^-$$
$$Co_3S_4OH^- + OH^- \leftrightarrow Co_3S_4O + H_2O + e^- \qquad (3)$$

From the measurements, CV curves are ascribed at various hydrothermal reaction temperatures with an occurrence of different peak currents. The charge storage capacity of the Co_3S_4 electrode is somewhat different for different reaction temperature and improved with the increase in reaction temperature. With the support of the surface microstructure of the Co_3S_4 electrode, different diffusion rates of electrons were observed along with electrode prepared at various reaction temperatures. The acceptable integrated area of the CV of the electrode was achieved at a reaction temperature of 120 °C. This may be due to the enhancement of more electroactive sites and because of the largely approachable surface areas that enable effective electrolyte ion transport during the redox operations, showing measurable electrochemical performance (Fig. 6(**b**) and (**c**)). Therefore, further

electrochemical testing was carried out with CS3 (hydrothermal reaction temperature of 120 °C) and subsequently with the Co_3S_4-rGO hybrid electrode.

4.1. Cyclic voltammetry (CV) studies

Cyclic voltammetry (CV) curves of the Co_3S_4 electrode are shown in Fig. 6(**d**) at different sweep scan rates (2, 5, 10, 20, 50, and 100 mV s^{-1}) in the potential range of −0.3–0.6 V vs SCE. The observed all cyclic voltammograms suggest that the Co_3S_4 electrode shows good reversibility of the oxidation and reduction processes. i.e. pseudo-capacitive characteristics, which differs from the electric double-layer capacitance characterized by nearly rectangular CV curves [42]. Also, as the scan rate increases, the anodic and cathodic peak potential shifts in the more positive and negative directions. The charge storage capability of the electrode is improved with the increment of area of the CVs, suggesting the merit of the elaborate architecture with the assistance of reduced graphene oxide. The thin nanosheets of reduced graphene oxide easily wrapped around the surfaces of the nanoflakes serve as a conductive supportive path with more surface area for the accompanying Co_3S_4 particles. Fig. 6(**e**) presents the CV profile of the Co_3S_4-rGO hybrid electrode at different scan rates. The symmetrical redox peaks at different scan rates imply the excellent reversible redox reaction at/near the surface of the Co_3S_4-rGO hybrid electrode. It is clearly seen that the redox peaks appeared in Co_3S_4-rGO shifted to the negative sides, resulting in a higher current than that of Co_3S_4 owing to the mass loading of the electrode material. The values of an areal capacitance at different scan rates are summarized in Fig. 6(**f**) for the Co_3S_4 and Co_3S_4-rGO hybrid electrodes, respectively. From the figures, it can be seen that the peak current density increases with increasing scan rate, which is perhaps due to the over potential for ion transport in the interface between the electrolyte and electrode. The gradual decrease of the capacitance values may be due to the charge resistive behavior of the electrode material at higher scan rates and to the diffusion ion charge transports lagging behind the electronic mobility [43]. The maximum areal capacitances of up to 6.95 F cm^{-2} for Co_3S_4 and 8.3 F cm^{-2} for Co_3S_4-rGO were obtained at a scan rate of 2 mV s^{-1}. This demonstrates that the prepared Co_3S_4-rGO hybrid electrode yields greatly improved capacitance performance of the Co_3S_4 electrode. Fig. 6(**g**) shows the values of specific capacitance based on the loading active mass of electrode materials against different scan rates. The estimated values of specific capacitances decreased with increasing scan rate. The Co_3S_4-rGO hybrid electrode exhibited an ultrahigh specific capacitance of 2314 F g^{-1} at 2 mV s^{-1} scan rate. Ramachandran et al. reported a maximum specific capacitance of 808 F g^{-1} at a scan rate of 5 mV s^{-1} for the Co_9S_8/G electrode prepared by using a simple chemical process. Chen et al. [44] reported the specific capacitance value of 2140 ± 90 F g^{-1} for the CNT/CoS composite electrode. For a hydrothermally prepared Ni@rGO-Co_3S_4 electrode, Ghosh et al. [14] reported a specific capacitance of 1369 F g^{-1}.

4.2. Galvanostatic charge-discharge studies

Fig. 6(**h**) shows a comparison of typical galvanostatic charge–discharge curves between the Co_3S_4 and Co_3S_4–rGO hybrid electrodes in the potential range of −0.3–0.6 V/SCE at a constant current density of 100 mA cm^{-2}. The charge-discharge rate of the Co_3S_4–rGO hybrid electrode is greater than that of the bare Co_3S_4 electrode. The good performance is attributed to the better electrical conductivity, increased surface area, and smaller pore size of the Co_3S_4–rGO electrode. The asymmetric behavior of the charge/discharge curve was interpreted as due to the redox reactions that
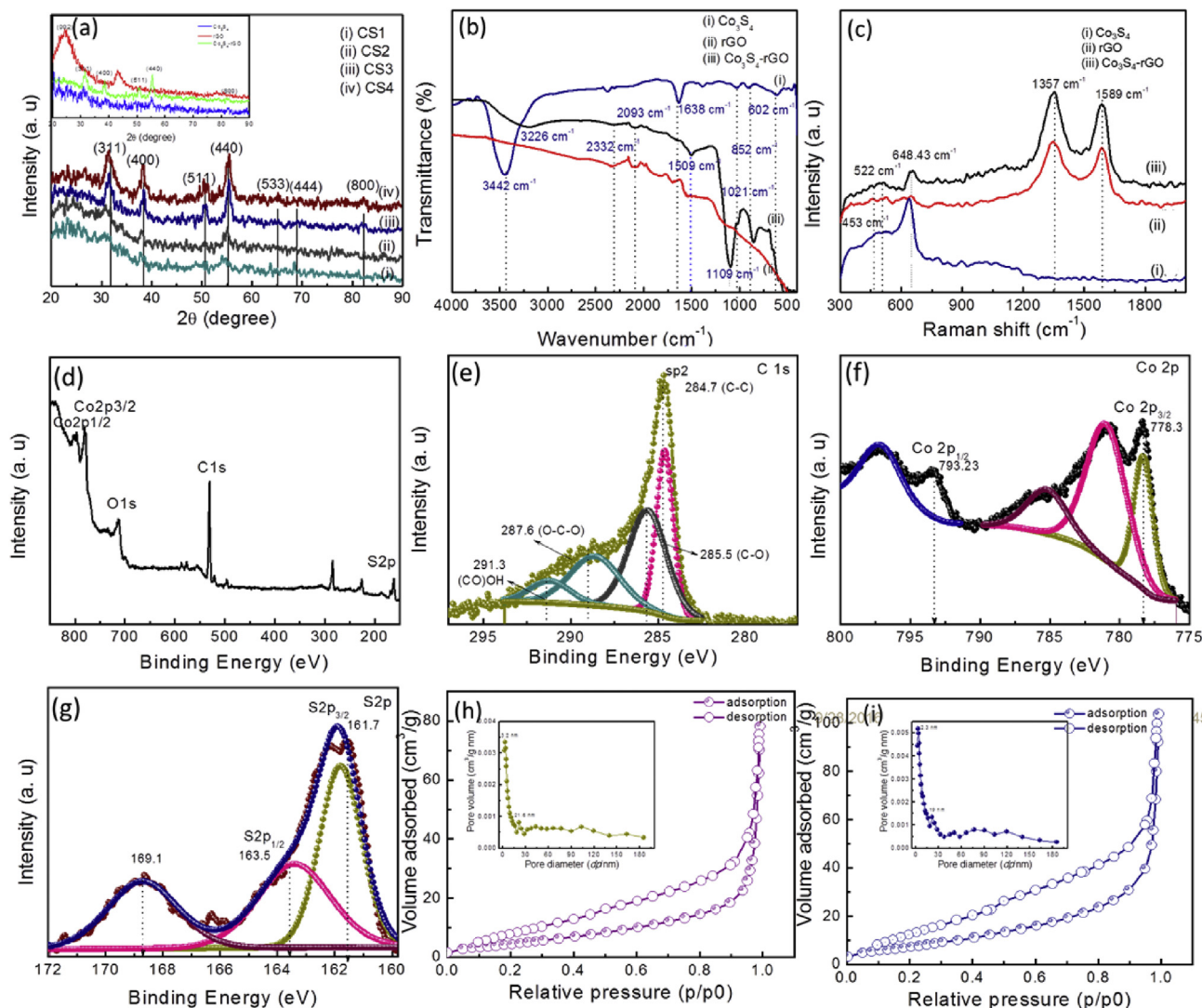
Fig. 5. Structural characterization: **(a)** XRD patterns of CS1, CS2, CS3 and CS4 and inset shows the XRD patterns for Co_3S_4, rGO and Co_3S_4-rGO. **(b)** FT-IR, and **(c)** Raman spectra of (i) Co_3S_4, (ii) rGO and (iii) Co_3S_4-rGO. XPS analyses of Co_3S_4-rGO; **(d)** full scan spectrum with **(e)** C1s, **(f)** Co 2p and **(g)** S 2p core spectrum. N_2 adsorption–desorption isotherms and inset show pore size distribution of **(h)** Co_3S_4 and **(i)** Co_3S_4-rGO material.

occur at the interface between the electrode and electrolyte. Fig. 6**(i)** and **(j)** show the charge/discharge profiles of the Co_3S_4 and Co_3S_4–rGO hybrid electrodes at various current densities in the potential range of −0.3–0.6 V/SCE. From the figure, it can be seen that the IR-drop increases with increase the current density, which is closely related to the charge transfer resistance (Rct) of the electrode. The discharging capacitance is calculated based on Equation (3); Fig. 6**(k)** displays the comparison of specific capacitance against the current density for both electrodes. The decreasing value of capacitance corresponding to the current density suggests that the surfaces of the electrodes are inaccessible at higher charge/discharge rates [6]. The Co_3S_4-rGO hybrid electrode exhibited a superior areal capacitance of 3.5 F cm^{-2} under a constant current density of 80 mA cm^{-2} compared to the multilayer-structured Ni/G/CS Nano-composite electrode (0.525 F cm^{-2} at a current density of 7.5 mA cm^{-2}) [17]. The maximum specific capacitance of 1293 F g^{-1} is associated with a lower IR-drop of the Co_3S_4-rGO hybrid electrode.

4.3. Ragone plot

The relation between energy density and power density is presented using the Ragone plot for the Co_3S_4 and Co_3S_4-rGO hybrid electrodes as shown in Fig. 6**(l)**, which depends on the calculated values of discharging specific capacitance. The Co_3S_4 electrode exhibits a maximum power density of 7.4 kW kg^{-1} and an energy density of 27.77 Wh kg^{-1} for the current densities of between 150 and 80 mA cm^{-2}, respectively. The Co_3S_4-rGO hybrid electrode exhibits a maximum energy density of 54.32 Wh kg^{-1}, which is higher than the Co_3S_4 electrode at a power density of 6.25 kW kg^{-1} (for the current densities of 80 mA cm^{-2}). In a comparison to other prepared single supercapacitor electrodes [45], the proposed electrodes demonstrated better performance in energy storage. Meanwhile, the obtained value of specific energy density is higher than that reported by Pujari et al. [46] for CoS_2 (40.74 Wh kg^{-1}) and by Liu et al. [47] for CoS_2/RGO/AC (45.7 Wh kg^{-1}).
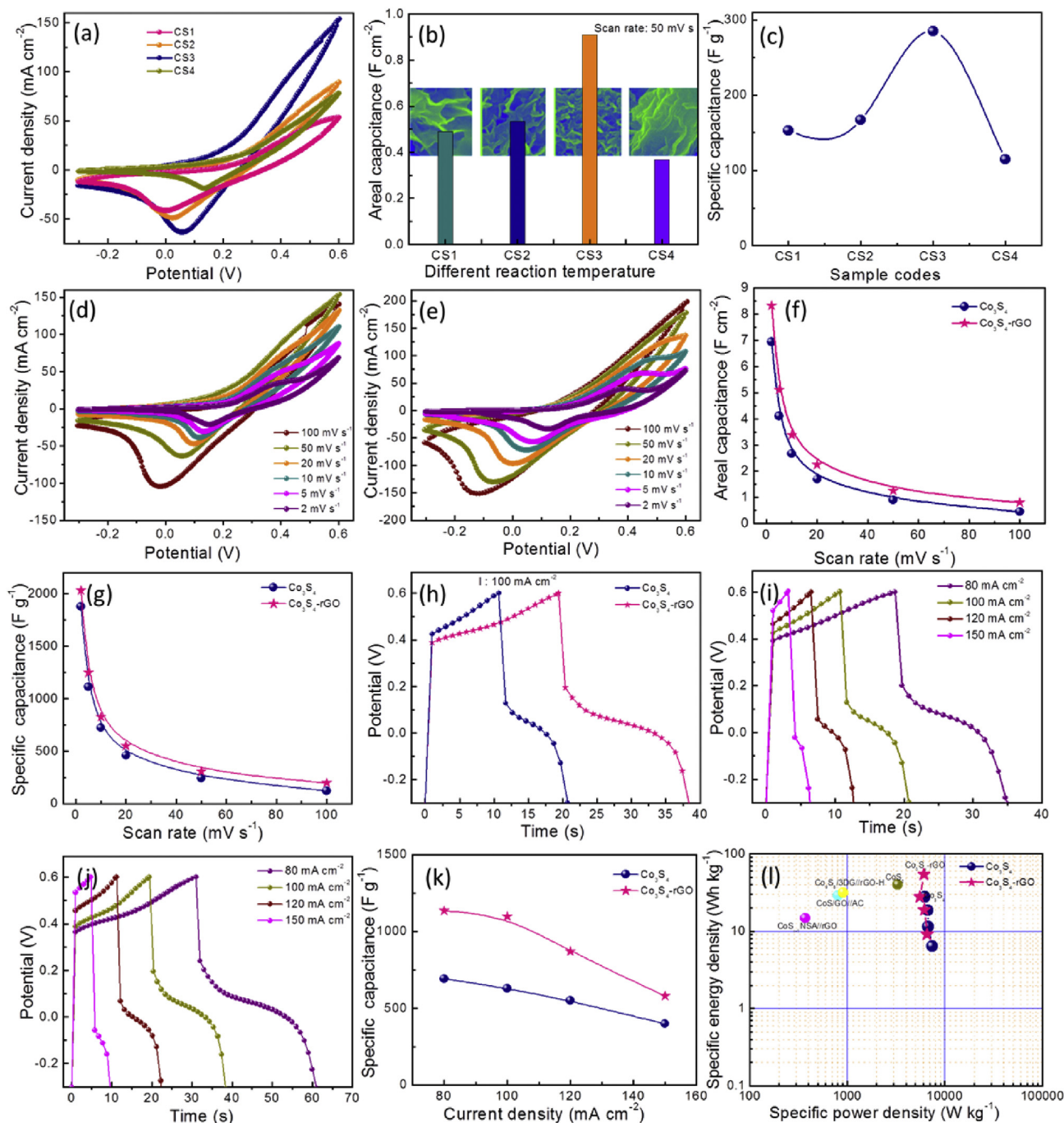
Fig. 6. Electrochemical performances of CS1, CS2, CS3, CS4 electrodes prepared at different reaction temperatures (80 °C, 100 °C, 120 °C, 160 °C); **(a)** cyclic voltammograms, **(b)** areal and **(c)** specific capacitance plots with constant scan rate of 50 mV s^{-1} **(d, e)** CV curves and plot of **(f)** areal and **(g)** specific capacitance at different scan rates ranging of; 2, 5, 10, 20, 50 and 100 mV s^{-1} in 2 M KOH electrolyte for Co_3S_4 and Co_3S_4-rGO hybrid electrode. Galvanostatic charge-discharge profile: **(h)** comparison of discharging curves at a constant current density of 100 mA cm^{-2}. Charge-discharge curves for **(i)** Co_3S_4, **(j)** Co_3S_4-rGO hybrid electrode, and **(k)** specific capacitance calculated from the corresponding discharge current densities. **(l)** Ragone plot for different discharging current densities.

4.4. Electrochemical cyclic stability studies

The cycling lifespan of the electrode material is an important parameter in electrochemical measurement. Here, we examined the electrochemical cyclic stability of Co_3S_4 and Co_3S_4-rGO hybrid electrodes by carrying out CV measurements at a scan rate of 100 mV s^{-1} over 1000 electrochemical cycles. The specific capacitive retention of the Co_3S_4 and Co_3S_4-rGO hybrid electrodes is shown in Fig. 7**(a)**, indicating the specific capacitance as a function

of cycle numbers. The CV profiles in the initial cycles appeared to be altered and achieved stable performance after several hundred cycles. The capacitive retention increase can be ascribed to that the electroactive process of Co_3S_4-rGO hybrid electrode will be more effective after the several charge-discharge cycles and enhancing capacitance. The capacitance losses are found to be 19.8% and 7.4% for the Co_3S_4 and Co_3S_4-rGO hybrid electrodes, respectively, after 1000 cycles. This suggests that after 1000 CV cycles, a superior cyclic stability is maintained for the Co_3S_4-rGO hybrid electrode
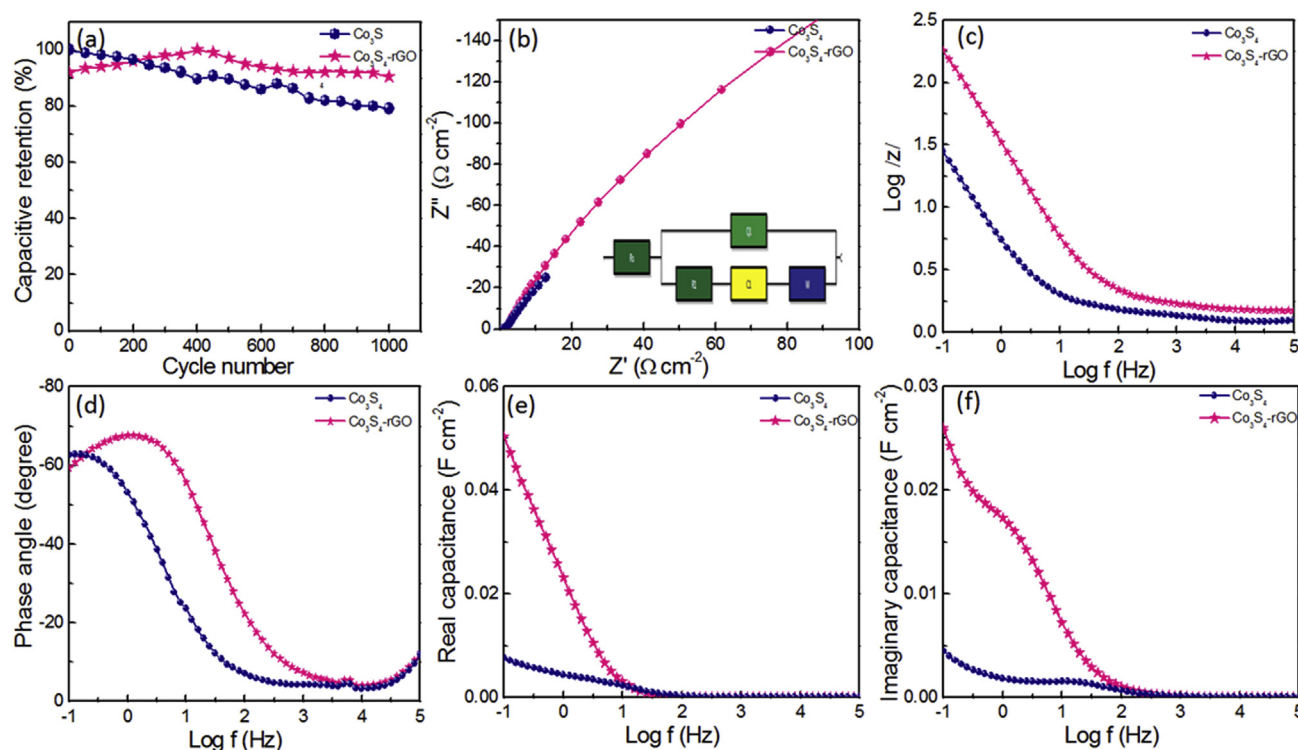
Fig. 7. **(a)** The capacitive retention with respect to CV cycles at 100 mV s^{-1} scan rate over 1000 cycles. Electrochemical impedance analyses of Co$_3$S$_4$ and Co$_3$S$_4$-rGO hybrid electrodes using a sinusoidal signal of 10 mV over 1 MHz to 0.1 Hz frequency range; **(b)** Nyquist plot (inset shows equivalent circuit used to fit the impedance data), **(c, d)** Bode magnitude and phase plots, **(e, f)** real and imaginary capacitance against frequencies.

without any significant mass change. Remarkably, the Co$_3$S$_4$ and Co$_3$S$_4$-rGO hybrid electrodes exhibited good electrochemical cyclic stability with 80.2% and 92.6% capacitive retention, respectively, of capacitance over 1000 cycles. The reduction in capacitive retention could be blocking the pores, possibly due to the initial CV cycles that induce a lower rate of ion adsorption. The nanosheet wrapped Co$_3$S$_4$-rGO hybrid electrode shows a better electrochemical capacitive retention than the Co$_9$S$_8$/RGO/Ni$_3$S$_2$/NF electrode (with 91.7% over 1000 cycles) [48]. Recently, Zeng et al. [49] reported a cycling stability of 71.7% for CoS@NiCo$_2$S$_4$ nanosheets arrays via a one-step ion exchange process.

4.5. Electrochemical impedance analyses

The electrochemical impedance measurements are performed in the potentiostatic mode to characterize the interface behavior of the Co$_3$S$_4$ and Co$_3$S$_4$-rGO electrodes with electrolyte solution. The variation of the real and imaginary components of the impedance data (Nyquist plot) is presented in Fig. 7(**b**) for the Co$_3$S$_4$ and Co$_3$S$_4$-rGO electrodes. The Nyquist plots suggest that the impedance curves are divided into the three main regions (low, middle, and high frequencies), wherein the Co$_3$S$_4$ and Co$_3$S$_4$-rGO hybrid electrodes in the low frequency region behave as an ideal capacitor with a vertical characteristic. In the intermediate frequency region, the Warburg element (W) represents the diffusion of electrolytic ions into the electrode material. The impedance data composed with the equivalent circuit model as shown in the inset in Fig. 7(**b**) and the corresponding parameter values for circuit elements summarized in Table 1. The circuit model composed of a solution resistance (Rs), charge-transfer resistance (Rct), double-layer capacitance (Cdl), Warburg diffusion resistance (W) and electrode surface dependence parameter (Q). Here, Rs is a solution resistance that arises from the combination of the bulk electrolyte resistance

Table 1
The equivalent circuit elements with parameter values.

Parameters	Co$_3$S$_4$	Co$_3$S$_4$-rGO
Rs	1.21	1.13
R1 (Rct)	3.14	1.18
C1 (Cdl)	0.03	0.04
W	1250	1115
Q	0.85	0.14

and contact resistance between the electroactive material and current collector. Rs values are found to be 1.21 and 1.13 Ω for Co$_3$S$_4$ and Co$_3$S$_4$-rGO hybrid electrodes, respectively. It is observed that the lower equivalent series resistance (ESR) of the Co$_3$S$_4$-rGO hybrid electrode improves the charge storage capacity compared to the Co$_3$S$_4$ electrode. The resulting comparatively smaller Rct (1.18 Ω) of Co$_3$S$_4$-rGO hybrid electrode should be associated with easy charge transfer and facilitate more interface contact area of the electrode/electrolyte. The Warburg diffusion resistance associated by diffusion of electrolyte ions around the electrode surface, 1250 Ω and 1115 Ω found to be Co$_3$S$_4$ and Co$_3$S$_4$-rGO hybrid electrodes. The double-layer capacitance (Cdl) is formed in the interface of electrolyte and electrode surface. The Bode magnitude plot is shown in Fig. 7(**c**) for both electrodes exhibits a straight line with a line slope of −1 and a change the phase angle in the low frequency region, indicating excellent capacitive characteristics with the fast charge transfer. The impedance phase angle of the Co$_3$S$_4$-rGO hybrid electrode reaches −90°, indicating a more supercapacitive behavior than the Co$_3$S$_4$ electrode shown in Fig. 7(**d**). The change in the real and imaginary components of the capacitance (C′ and C″) versus frequency are presented in Fig. 7(**e**) and (**f**) for the Co$_3$S$_4$ and Co$_3$S$_4$-rGO hybrid electrodes, respectively. The real component of the capacitance, C′, sharply decreases with frequency. The plot of C″

against frequency shows that C″ gives a relaxation time constant ($\tau_0 = 1/f_m$) where it represents the transition of the supercapacitor between the resistive and capacitive behavior of the electrode material. The relaxation time constant is found to be 0.66 s and 0.05 s for the Co_3S_4 and Co_3S_4-rGO hybrid electrodes, respectively, which is the lowest time constant attributed to rapidly achieve power during discharging. The different relaxation time constant could be due to the microstructural change of the electrode and the role of graphene in power performance.

5. Asymmetric supercapacitor fabrication and performance evaluation

The asymmetric supercapacitor was fabricated using Co_3S_4 and Co_3S_4-rGO as a positive and negative electrode, respectively. The typical total loading mass of the active electrode material for the asymmetric supercapacitor assembly is about 4.7 mg. The mass loading (m) of the two electrode materials was balanced before making the supercapacitors assembly, and the actual weight of each electrode material was estimated according to the specific capacitance (C) calculated from the cyclic voltammetry curves in a three-electrode system by maintaining a 1.2 V potential window (ΔV). Equation (4) is used to obtain the mass ratio between the positive and negative electrodes:

$$\frac{m_-^{\,-}}{m_+} = \frac{c_{m-} \times \Delta V}{c_{m+} \times \Delta V} \tag{4}$$

Further, the electrochemical performances of the prepared asymmetric supercapacitor device are studied in the PVA/KOH gel-electrolyte. The usage of PVA/KOH gel-electrolyte can avoid the main drawbacks of conventional liquid electrolytes such as difficulty in device integration and the leakage of electrolyte, environmental stability, etc. PVA/KOH gel-electrolyte was prepared by the following process: 6 g of PVA was dissolved in 50 ml DI water under vigorous stirring and heating for 1 h. Then, 4 g of KOH was added in 5 ml DI water and then mixed with the previously prepared PVA solution. The mixture was vigorously stirred until the solution became clear. The polymeric gel-electrolyte was obtained after cooling the solution. The asymmetric solid-state supercapacitor was fabricated by assembling two identical pieces of the Co_3S_4 and Co_3S_4-rGO electrodes with a sandwiched polymeric gel-electrolyte. Further, the fabricated device assembly was kept in the oven at 60° to vaporize the excess water in the gel-electrolyte.

The various CV measurements for the Co_3S_4/Co_3S_4-rGO asymmetric supercapacitor are performed in different potential windows (from 1.2 V to 1.6 V) at a fix scan rate of 100 mV s^{-1} as shown in Fig. 8(**a**) and the inset illustrate the cyclic voltammograms. The fabricated supercapacitor assembly reveals that, rGO nanosheets responsible for leading the potential of cell. The electrochemical measurements are shown in Fig. 8(**b**) was tested in 0−1.5 V voltage range; the CV behavior of the fabricated asymmetric supercapacitor is performed with different scanning rates ranging from 2 to 200 mV s^{-1}. Fig. 8(**c**) suggests the obtained values of the areal and specific capacitance of a fabricated asymmetric supercapacitor, which are plotted with respect to scan rates. The values of specific capacitance are calculated to be 36, 14, and 5 F g^{-1} for the scan rates of 2, 10, and 200 mV s^{-1}, respectively. Hence, the specific capacitance obtained at the slow scan rates is conceived to be closest to that of full utilization of the electrode material. Analogous shapes of CV curves are clearly shown, revealing hybrid supercapacitor behaviors.

Moreover, the charge/discharge profiles at different current densities of 2 mA cm^{-2}, 3 mA cm^{-2} and 4 mA cm^{-2} are presented in Fig. 8(**d**). The prepared Co_3S_4-rGO based asymmetric

supercapacitor shows nearly symmetric behavior with a high rate of charge/discharge. The areal capacitance of 14, 10, and 3 mF cm^{-2} were obtained at a discharge current density of 2, 3, and 4 mA cm^{-2}, respectively, for asymmetric supercapacitor assembly. The Ragone plot (Fig. 8(**e**)) shows that the energy density of the asymmetric supercapacitor decreases from 1.09 to 0.31 Wh kg^{-1}, whereas the power density for the asymmetric supercapacitor increases from 398 to 750 W kg^{-1}, as the discharge current increased from 2 mA cm^{-2} to 4 mA cm^{-2}. Liu et al. [35] demonstrated a solid-state asymmetric supercapacitor composed of $Co_3O_4@Co_3S_4$ and the activated carbon (AC) electrodes exhibited an energy density of 1.5 mWh cm^{-3} and power density of 6.1 W cm^{-3}. Also, Xu et al. [50] demonstrated that the solid-state electrolyte based asymmetric supercapacitor device ($Co_9S_8/Co_3O_4@RuO_2$) performed in the potential range from 0 to 1.6 V exhibited an energy density of 1.44 mWh cm^{-3} at the power density of 0.89 W cm^{-3}. The literature survey reveals that the fabricated Co_3S_4/Co_3S_4-rGO supercapacitor device used in present works demonstrated acceptable values of energy and power density even at lower discharge current density. Eventually, the long-term cyclic stability of the fabricated device was investigated for 5000 CVs cycles with a high scan rate of 100 mV s^{-1}. The capacitive retention versus cycle numbers as shown in Fig. 8(**f**) demonstrates excellent CV cyclic stability with the capacitive retention of 89.56% of the initial capacitance for 5000 cycles. Inset figure shows the cyclic voltammograms for several CV cycles. The area under the curve of the asymmetric supercapacitor initially slightly decreases (up to 800 cycles) and then becomes constant without loss of capacitance, increased capacitive retention can attribute to the activation of electroactive sites during earlier CV cycles. Importantly, initial 2000 CV cycles, 96.13% capacitive retention observed where it shows that no significant change of degradation occurred in the charge storage capacity. The observed capacitive retention is much better than that previously reported for CoS_x-NSA (84% for 3000 cycles) [51], CoS@eRG (70% for 10,000 cycles) [52], and Co_9S_8/3D (86% for 6000 cycles) [53] asymmetric supercapacitors.

The Nyquist plot presented in Fig. 8(**g**) for asymmetric supercapacitor devices based on the Co_3S_4/Co_3S_4-rGO electrode shows an almost vertical line in a low frequency region, reflecting the good electrical conductivity of the electrode as well as its excellent charge storage rate capability. Also, in the higher frequency region, the line intersecting the real axis at an angle of 45° implies that electrolyte ions have a fast rate of ion diffusion in the porous electrode surface. Inset of Fig. 8(**g**) shows a fitted equivalent circuit model with smaller ESR (4.2 Ω) attributed to the lower internal resistance of the cell assembly and ensures fast ion accessibility for adsorption and desorption. The impedance phase angle and magnitude plots for the asymmetric supercapacitor at different frequencies are plotted in Fig. 8(**h**), and the phase angle reaches −90° behaves as a capacitive nature. The phase angle of −82° was obtained for the Co_3S_4/Co_3S_4-rGO asymmetric supercapacitor device, indicating pseudocapacitive behavior [7]. The real and imaginary components of the capacitances decrease with frequency (Fig. 8(**i**)). From the peak imaginary capacitance (C″) frequency (f_m), the relaxation time constant (τ_0) is calculated to be 625 μs, attributed to the minimum time required to discharge the device.

6. Conclusions

In summary, the Co_3S_4 and Co_3S_4-rGO hybrid structures were successfully prepared via an easy effective two-step hydrothermal method on Ni-foam. The two-step process was followed to vary the reaction temperature for sulfidation, which strongly affected the electrochemical and physical properties of the Co_3S_4
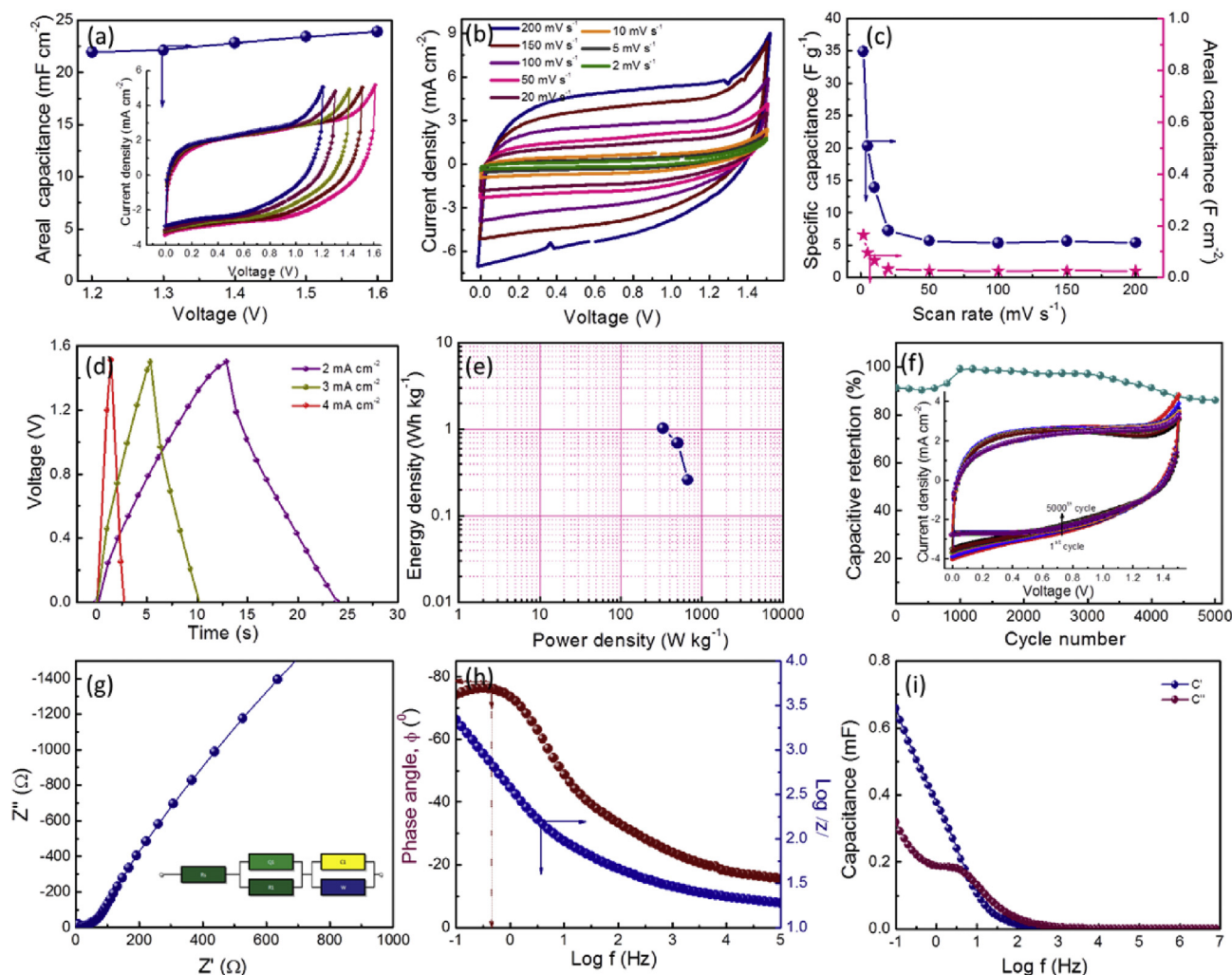
Fig. 8. Electrochemical characteristics of asymmetric supercapacitor device fabricated based on polymeric gel electrolyte: **(a)** the values of areal capacitance with optimized voltage window variations and inset shows corresponding CV curves, **(b)** CV curves in the voltage range of 0—1.5 V with scan rate ranging from 2 to 200 mV s^{-1}, **(c)** areal and specific capacitance as function of scan rates. **(d)** The charge—discharge profiles of asymmetric supercapacitor device collected at different current densities of 2 mA cm^{-2}, 3 mA cm^{-2} and 4 mA cm^{-2}, and corresponding plot dissipated as **(e)** the relation between energy and power densities (Ragone plot). The cyclic stability study carried out at 100 mV s^{-1} scan rate: **(f)** the capacitive retention as a function of cycle number over 5000 cycles and inset shows CV curves for different cycles. **(g—i)** Impedance analyses of asymmetric supercapacitor device.

electrode material. Further, rGO nanosheets wrapped around the Co$_3$S$_4$ nanoflake hybrid electrode was prepared to improve the energy storage capability. The ultrahigh value of areal and specific capacitance of 8.33 F cm^{-2} and 2314 F g^{-1}, respectively are observed for Co$_3$S$_4$-rGO hybrid electrode at 2 mV s^{-1} scan rate. The Co$_3$S$_4$ nanoflakes exhibited an energy density of 27.77 Wh kg^{-1} and a greatly enhanced energy density of up to 54.32 Wh kg^{-1} with the Co$_3$S$_4$-rGO hybrid electrode at a galvanostatic charge-discharge current density of 80 mA cm^{-2}. The lightweight asymmetric solid-state supercapacitor assembly based on Co$_3$S$_4$ and Co$_3$S$_4$-rGO electrodes was fabricated and showed acceptable values of specific capacitance (36 F g^{-1}) with good electrochemical cycle stability (89.56% up to 5000 cycles). The electrochemical performance of the asymmetric supercapacitor is mainly due to the synergic effect from the redox reactions for the Co$_3$S$_4$ nanoflakes and the excellent electron transfer ability for rGO nanosheets. The electrochemical characterization shows that the Co$_3$S$_4$ nanoflakes based hybrid electrode exhibits excellent electrochemical activities.

References

[1] A. González, E. Goikolea, J.A. Barrena, R. Mysyk, Review on supercapacitors: technologies and materials, Renew. Sustain. Energy Rev. 58 (2016) 1189—1206.
[2] H. Zhang, H. Su, L. Zhang, B. Zhang, F. Chun, X. Chu, W. He, W. Yang, Flexible supercapacitors with high areal capacitance based on hierarchical carbon tubular nanostructures, J. Power Sources 331 (2016) 332—339.
[3] G. Wang, L. Zhang, J. Zhang, A review of electrode materials for electrochemical supercapacitors, Chem. Soc. Rev. 41 (2012) 797—828.
[4] J. Yang, X. Duan, Q. Qin, W. Zheng, Solvothermal synthesis of hierarchical flower-like b-NiS with excellent electrochemical performance for supercapacitors, J. Mater. Chem. A 1 (2013) 7880—7884.
[5] R. Ramachandran, M. Saranya, C. Santhosh, V. Velmurugan, B.P.C. Raghupathy, S.K. Jeong, A.N. Grace, Co9S8 nanoflakes on graphene (Co9S8/G) nanocomposites for high performance supercapacitors, RSC Adv. 4 (2014) 21151—21162.

[6] S.J. Patil, C.D. Lokhande, Fabrication and performance evaluation of rare earth lanthanum sulfide film for supercapacitor application: effect of air annealing, Mater. Des. 87 (2015) 939–948.

[7] K. Krishnamoorthy, P. Pazhamalai, G.K. Veerasubramani, S.J. Kim, Mechanically delaminated few layered MoS2 nanosheets based high performance wire type solid-state symmetric supercapacitors, J. Power Sources 321 (2016) 112–119.

[8] X. Xiong, G. Waller, D. Ding, D. Chen, B. Rainwater, B. Zhao, Z. Wang, M. Liu, Controlled synthesis of NiCo2S4 nanostructured arrays on carbon fiber paper for high-performance pseudocapacitors, Nano Energy 16 (2015) 71–80.

[9] J. Chen, Y. Huang, C. Li, X. Chen, X. Zhang, Synthesis of NiO@MnO2 core/shell nanocomposites for supercapacitor application, Appl. Surf. Sci. 360 (2016) 534–539.

[10] S. Liu, C. Mao, Y. Niu, F. Yi, J. Hou, S. Lu, J. Jiang, M. Xu, C. Li, Facile synthesis of novel networked ultralong cobalt sulfide nanotubes and its application in supercapacitors, ACS Appl. Mater. Interfaces 7 (2015) 25568–25573.

[11] C. Gea, X. Zhanga, J. Liua, F. Jina, J. Liub, H. Bi, Hollow-spherical composites of Polyaniline/Cobalt Sulfide/Carbon nanodots with enhanced magneto-capacitance and electromagnetic wave absorption capabilities, Appl. Surf. Sci. 378 (2016) 49–56.

[12] B. You, N. Jiang, M. Sheng, Y. Sun, Microwave vs. solvothermal synthesis of hollow cobalt sulfide nanoprisms for electrocatalytic hydrogen evolution and supercapacitors, Chem. Commun. 51 (2015) 4252–4255.

[13] S. Xie, Y. Deng, J. Mei, Z. Yang, W.-M. Lau, H. Liu, Facile synthesis of CoS2/CNTs composite and its exploitation in thermal battery fabrication, Compos. Part B 93 (2016) 203–209.

[14] D. Ghosh, C.K. Das, Hydrothermal growth of hierarchical Ni3S2 and Co3S4 on a reduced graphene oxide Hydrogel@Ni foam: a high-energy-density aqueous asymmetric supercapacitor, ACS Appl. Mater. Interfaces 7 (2015) 1122–1131.

[15] Q. Chen, H. Li, C. Cai, S. Yang, K. Huang, X. Wei, J. Zhong, In situ shape and phase transformation synthesis of Co3S4 nanosheet arrays for high-performance electrochemical supercapacitors, RSC Adv. 3 (2013) 22922–22926.

[16] X. Meng, J. Deng, J. Zhu, H. Bi, E. Kan, X. Wang, Cobalt sulfide/graphene composite hydrogel as electrode for high-performance pseudocapacitors, Sci. Rep. 6 (2016) 21717.

[17] Q.F. Zhang, C.M. Xu, B.G. Lu, Super-long life supercapacitors based on the construction of Ni foam/graphene/Co3S4 composite film hybrid electrodes, Electrochim. Acta 132 (2014) 180–185.

[18] I. Bilecka, M. Niederberger, Microwave chemistry for inorganic nanomaterials synthesis, Nanoscale 2 (2010) 1358–1374.

[19] X.H. Xia, D.L. Chao, Y.Q. Zhang, Z.X. Shen, H.J. Fan, Three-dimensional graphene and their integrated electrodes, Nano Today 9 (2014) 785–807.

[20] Y. Zhu, S. Murali, W. Cai, X. Li, J.W. Suk, J.R. Potts, R.S. Ruoff, Graphene and graphene oxide: synthesis, properties, and applications, Adv. Mater. 22 (2010) 3906–3924.

[21] X. Dong, W. Huang, P. Chen, In situ synthesis of reduced graphene oxide and gold nanocomposites for nanoelectronics and biosensing, Nanoscale Res. Lett. 6 (2011) 60.

[22] S.Q. Chen, Y. Wang, Microwave-assisted synthesis of a Co 3 O 4–graphene sheet-on-sheet nanocomposite as a superior anode material for Li-ion batteries, J. Mater. Chem. 20 (2010) 9735–9739.

[23] J. Liu, Y. Xing, X. Liu, X. Yu, Z. Su, Hydrothermal synthesis and magnetic properties of nanoplate-assembled hierarchical structured Co1-xS microrods, Mater. Charact. 67 (2012) 112–118.

[24] J. Zhang, W. Yang, J. Liu, Facile fabrication of supercapacitors with high rate capability using graphene/nickel foam electrode, Electrochim. Acta 209 (2016) 85–94.

[25] J. Shi, X. Li, G. He, L. Zhang, M. Li, Electrodeposition of high-capacitance 3D CoS/graphene nanosheets on nickel foam for high-performance aqueous asymmetric supercapacitors, J. Mater. Chem. A 3 (2015) 20619–20626.

[26] X. Liu, N. Wen, X. Wang, Y. Zheng, Layer-by-Layer self-assembled graphene multilayer films via covalent bonds for supercapacitor electrodes, Nanomater. Nanotechnol. 5 (2015) 14, http://dx.doi.org/10.5772/60596.

[27] M. Lei, R. Zhang, H.J. Yang, Y.G. Wang, Synthesis of well dispersed cobalt di-sulfide and their photoluminescence and magnetic properties, Mater. Lett. 76 (2012) 87–89.

[28] J. Huo, J. Wu, M. Zheng, Y. Tu, Z. Lan, High performance sponge-like cobalt sulfide/reduced graphene oxide hybrid counter electrode for dye-sensitized solar cells, J. Power Sources 293 (2015) 570–576.

[29] K.-J. Huang, Y.-J. Liu, J.-Z. Zhang, J.-T. Cao, Y.-M. Liu, High performance sponge-like cobalt sulfide/reduced graphene oxide hybrid counter electrode for dye-

[30] sensitized solar cells, Biosens. Bioelectron. 67 (2015) 184–191.

[30] F. Tuinstra, J.L. Koenig, Raman spectrum of graphite, J. Chem. Phys. 53 (1970) 1126–1130.

[31] L.M. Malard, M.A. Pimenta, G. Dresselhaus, M.S. Dresselhaus, Raman spectroscopy in graphene, Phys. Rep. 473 (2009) 51.

[32] J. He, Y. Chen, P. Li, F. Fu, Z. Wang, W. Zhang, Self-assembled CoS2 nanoparticles wrapped by CoS2-quantum-dots-anchored graphene nanosheets as superior-capability anode for lithium-ion batteries, Electrochim. Acta 182 (2015) 424–429.

[33] R. Zou, Z. Zhang, M.F. Yuen, J. Hu, C. Lee, W. Zhang, Sci. Rep. 5 (2015) 1.

[34] S. Some, Y. Kim, E. Hwang, H. Yoo, H. Lee, Binol salt as a completely removable graphene surfactant, Chem. Commun. 48 (2012) 7732–7734.

[35] B. Liu, D. Kong, J. Zhang, Y. Wang, T. Chen, C. Cheng, H.Y. Yang, 3D hierarchical Co3O4@Co3S4 nanoarrays as cathode materials for asymmetric pseudocapacitors, J. Mater. Chem. A 4 (2016) 3287–3296.

[36] P. Ganesan, M. Prabu, J. Sanetuntikul, S. Shanmugam, Cobalt sulfide nanoparticles grown on nitrogen and sulfur codoped graphene oxide: an efficient electrocatalyst for oxygen reduction and evolution reactions, ACS Catal. 5 (2015) 3625–3637.

[37] S. Das, P. Sudhagar, S. Nagarajan, E. Ito, S.Y. Lee, Y.S. Kang, W. Choi, Synthesis of graphene-CoS electro-catalytic electrodes for dye sensitized solar cells, Carbon 50 (2012) 4815–4821.

[38] M. Liu, X. Wang, D. Zhu, L. Li, H. Duan, Z. Xu, Z. Wang, L. Gan, Encapsulation of NiO nanoparticles in mesoporous carbon nanospheres for advanced energy storage, Chem. Eng. J. 308 (2017) 240–247.

[39] M. Liu, X. Ma, L. Gan, Z. Xu, D. Zhu, L. Chen, A facile synthesis of a novel mesoporous Ge@C sphere anode with stable and high capacity for lithium ion batteries, J. Mater. Chem. A 2 (2014) 17107–17114.

[40] Z.L. Zhao, H.X. Wu, H.L. He, X.L. Xu, Y.D. Jin, A high-performance binary Ni-Co hydroxide-based water oxidation electrode with three-dimensional coaxial nanotube array structure, Adv. Funct. Mater. 24 (2014) 4698–4705.

[41] J.-C. Xing, Y.-L. Zhu, Q.-W. Zhou, X.-D. Zheng, Q.-J. Jiao, Fabrication and shape evolution of CoS2 octahedrons for application in supercapacitors, Electrochim. Acta 136 (2014) 550–556.

[42] H. Pang, C. Wei, X. Li, G. Li, Y. Ma, S. Li, J. Chen, J. Zhang, Microwave-assisted synthesis of NiS2 nanostructures for supercapacitors and cocatalytic enhancing photocatalytic H2 production, Sci. Rep. 4 (2014) 3577.

[43] N.K. Sidhu, A.C. Rastogi, Bifacial carbon nanofoam-fibrous PEDOT composite supercapacitor in the 3-electrode configuration for electrical energy storage, Syn. Met. 219 (2016) 1–10.

[44] C.-Y. Chen, Z.-Y. Shih, Z. Yang, H.-T. Chang, Carbon nanotubes/cobalt sulfide composites as potential high-rate and high-efficiency supercapacitors, J. Power Sources 215 (2012) 43–47.

[45] Q. Wang, L. Jiao, H. Du, J. Yang, Q. Huan, W. Peng, Y. Si, Y. Wang, H. Yuan, Facile synthesis and superior supercapacitor performances of three-dimensional cobalt sulfide hierarchitectures, CrystEngComm 13 (2011) 6960–6963.

[46] R.B. Pujari, A.C. Lokhande, J.H. Kim, C.D. Lokhande, Bath temperature controlled phase stability of hierarchical nanoflakes CoS2 thin films for supercapacitor application, RSC Adv. 6 (2016) 40593.

[47] G. Liu, B. Wang, L. Wang, Y. Yuan, D. Wang, A facile hydrothermal synthesis of a reduced graphene oxide modified cobalt disulfide composite electrode for high-performance supercapacitors, RSC Adv. 6 (2016) 7129–7138.

[48] Z. Zhang, Q. Wang, C. Zhao, S. Min, X. Qian, One-step hydrothermal synthesis of 3D petal-like Co9S8/RGO/Ni3S2 composite on nickel foam for high-performance supercapacitors, ACS Appl. Mater. Interfaces 7 (2015) 4861–4868.

[49] W. Zeng, G. Zhang, X. Wu, K. Zhang, H. Zhang, S. Hou, C. Li, T. Wang, H. Duan, Construction of hierarchical CoSnanowire@NiCo2S4nanosheet arraysviaone-step ion exchange for high-performance supercapacitors, J. Mater. Chem. A 3 (2015) 24033–24040.

[50] J. Xu, Q. Wang, X. Wang, Q. Xiang, B. Liang, D. Chen, G. Shen, Flexible asymmetric supercapacitors based upon Co9S8 Nanorod//Co3O4@RuO2 nanosheet arrays on carbon cloth, ACS Nano 7 (2013) 5453–5462.

[51] D.P. Dubal, G.S. Gund, C.D. Lokhande, R. Holze, Controlled growth of CoSx nanostrip arrays (CoSx@NSA) on nickel foam for asymmetric supercapacitors, Energy Technol. 2 (2014) 401–408.

[52] J. Shi, X. Li, G. He, L. Zhang, M. Li, Electrodeposition of high-capacitance 3D CoS/graphene nanosheets on nickel foam for high-performance aqueous asymmetric supercapacitors, J. Mater. Chem. A 3 (2015) 20619–20626.

[53] T.-W. Lin, C.-S. Dai, T.-T. Tasi, S.-W. Chou, J.-Y. Lin, H.-H. Shen, High-performance asymmetric supercapacitor based on Co9S8/3D graphene composite and graphene hydrogel, Chem. Eng. J. 279 (2015) 241–249.